

Complex-domain Joint Broadband Hyperspectral Image Denoising

¹ Vladimir KATKOVNIK, ^{1,*} Igor SHEVKUNOV, ² Daniel CLAUS,
³ Giancarlo PEDRINI, ¹ Karen EGIAZARIAN

¹ Tampere University, Faculty of Information Technology and Communication Sciences,
Korkeakoulunkatu 10, 33101 Tampere, Finland

² Institut für Lasertechnologien in der Medizin und Messtechnik,
Helmholtzstraße 12, 89081 Ulm, Germany

³ Institut für Technische Optik (ITO), Universität Stuttgart,
Pfaffenwaldring 9, 70569 Stuttgart, Germany

*Tel.: +358 3 311 511

*E-mail: igor.shevkunov@tuni.fi

Received: 30 March 2019 /Accepted: 30 April 2019 /Published: 31 May 2019

Abstract: In this paper, we propose a novel complex domain denoising algorithm for hyperspectral data. The algorithm is based on the Complex Domain Block-Matching 3D (CDBM3D) filter and on similarity of hyperspectral data, which are usually slow varying for close values of wavelengths. Singular Value Decomposition (SVD) of the hyperspectral data is used in order to define an optimal small dimension data subspace. The CDBM3D is applied for 2D images of this subspace. The efficiency of the algorithm is demonstrated in simulation tests and for experimental data obtained by spectrally resolved digital holography of a transparent color object. It is proved that the proposed filtering algorithm retrieves amplitude and phase distributions even from very noisy data.

Keywords: Hyperspectral imaging, Noise in imaging systems, Complex domain imaging, Complex domain sparsity.

1. Introduction

Hyperspectral imaging (HSI) is originated from the earth remote sensing [1] and widely explored for numerous applications, including control of water and vegetation resources, control of food quality, biomedicine [2], etc. Acquiring two-dimensional (2D) images across a wide range of electromagnetic spectra with hundreds or thousands of spectral channels, HSI provides valuable information on material, size, shape and other characteristics of objects of interest.

Conventionally, 2D measured hyperspectral (HS) images are stacked together and represented as 3D

cubes with the spatial coordinates (x,y) and the third coordinate for wavelength λ or for frequency ω . In practice, the potential of HSI is compromised by low quality of the registered 2D images due to various degradation mechanisms.

Recently, HSI has received great attention in the field of digital holography (DH), which enables reconstruction both HS intensity and HS phase (e.g. [6-8]). In this case, the hyperspectral cubes are complex valued, i.e. each of 2D wavelength slices of the 3D cube is characterized by phase and amplitude. The phase reconstruction provides a possibility to get additional information on refractive index and/or

thickness of an investigated object in a single wavelength [9] and multispectral [10-11] scenarios.

In digital holography, reconstructed complex-valued images are obtained from indirect intensity observations as solutions of ill-posed inverse problems. The later leads to serious amplification of noisy components in HS data, in particular, as speckle effects in phase images.

An averaging of 2D slices of HS cubes by the windowed sliding sample mean over the wavelength axis is used routinely for denoising [6-7]. This approach is able to filter out the noise but may result in serious oversmoothing of the clean signal, in particular if the wavelength window size is too large. An application of the more sophisticated BM3D (Block-Matching 3D) algorithm with separate filtering of phase and amplitude is appeared to be more efficient than the sliding sample means [12].

This paper reports development of instruments for joint broadband processing of correlated phase and amplitude of complex valued HS images. This joint processing allows achieving essentially better results than those based on data processing separate for each wavelength. Singular Value Decomposition (SVD) of the complex valued hyperspectral images are used in order to identify a small number of 2D eigenimages. The original Complex Domain Block-Matching 3D (CDBM3D) filters are used for filtering of these complex valued eigenimages. This paper is a further development of the results shown in our conference paper [13].

2. Problem Formulation and Algorithm

Let $U(x, y, \lambda) \in \mathbb{C}^{N \times M}$ be a 2D slice of the HS noisy cube having size $N \times M$ in (x, y) coordinates with a fixed wavelength λ . $Q_\Lambda(x, y, \lambda_0) = \{U(x, y, \lambda), \lambda_0 - \delta_{\lambda_0}/2 \leq \lambda \leq \lambda_0 + \delta_{\lambda_0}/2\}$, $Q_\Lambda \in \mathbb{C}^{N \times M \times L_\Lambda}$, is a group of the slices (HS cube) belonging, for instance, to the wavelength interval of width δ_{λ_0} centered on λ_0 . The rows of $Q_\Lambda(x, y, \lambda_0)$ contain L_Λ spectral observations corresponding to the scene with coordinate (x, y) .

Observations of the HS denoising problem under the additive noise assumption may be written as

$$Z_\Lambda(x, y) = Q_\Lambda(x, y) + \varepsilon_\Lambda(x, y), \quad (1)$$

where $Z_\Lambda, Q_\Lambda, \varepsilon_\Lambda \in \mathbb{C}^{N \times M \times L_\Lambda}$ represent the observed noisy HS data, clean HS data and additive noise, respectively.

The denoising is formulated as reconstruction of the unknown $Q_\Lambda(x, y)$ from given $Z_\Lambda(x, y)$. The properties of the clean HS $Q_\Lambda(x, y)$ and the noise $\varepsilon_\Lambda(x, y)$ are essential for algorithm development.

The following three assumptions are basic hereafter.

1. Similarity of the HS slices $U(x, y, \lambda)$ for close values of λ follows from the fact that $U(x, y, \lambda)$ usually are slowly varying functions of λ . Then, for the

set of spectral images $Q_\Lambda(x, y)$ of the length L_Λ , there exists a k -dimensional subspace with $k \ll L_\Lambda$. Therefore, there is a linear transform E reducing the size of the cube $Q_\Lambda(x, y)$ to the cube of smaller size. Following [14], we herein term the images associated with this k -dimensional subspace as eigenimages. A smaller size of this subspace automatically means a potential to improve the HS denoising being produced in this subspace.

2. A sparsity of HS images $U(x, y, \lambda)$ as functions of (x, y) means that there is a basis such that $U(x, y, \lambda)$ can be represented with a small number of atoms of this basis. It is one of the conventional and fundamental assumptions for design of modern image processing algorithms. The sparsity concept for complex valued images is quite different from the standard formulation of this concept for real-valued signals. In particular, it is because the complex valued variables can be defined also by any of the two pairs: amplitude/phase or real/imaginary values of complex variables and elements of these pairs can be correlated [15-16].

3. The noise $\varepsilon_\Lambda(x, y)$ is circular zero mean i.i.d. Gaussian.

3. Proposed Algorithms

We present and demonstrate two types of the algorithms: separate and joint denoising of HS cube slices.

3.1. Separate Denoising of HS Cube Slices

The algorithms of this group filter the images of the HS cube for each wavelength slice separately with results, which can be shown as:

$$\hat{U}(x, y, \lambda) = \text{CDBM3D}(Z(x, y, \lambda)), \lambda \in \Lambda, \quad (2)$$

where CDBM3D is the abbreviation for Complex Domain Block-Matching 3D filter [15] and $\hat{U}(x, y, \lambda)$ is the estimate of the true unknown wavefront $U(x, y, \lambda)$. The MATLAB codes of this algorithm are publicly available: <http://www.cs.tut.fi/sgn/imaging/sparse/>. A further development of these algorithms for complex domain filtering can be seen in [16-18]. Each of these new algorithms can be applied for filtering in (2).

The CDBM3D algorithm is a generalization for the complex-domain of the popular real-valued Block-Matching 3D (BM3D) filters [19]. Two points define the potential advantage of CDBM3D in comparison, in particular, with using BM3D separately for phase and amplitude as is in [12, 20]. First, CDBM3D processes phase and amplitude jointly taking into consideration a correlation of these variables usual in most applications, while separate filtering of amplitude and phase ignores this correlation. Second, the basic functions used in BM3D are fixed, while in CDBM3D they are varying data adaptive making estimation more precise.

The BM3D and CDBM3D algorithms are based on nonlocal similarity of small patches of images always existing in real-live data. The algorithms look for similar patches, identify them, stack together and process as 3D arrays. This similarity concept allows to use the powerful modern tools of sparse approximations allowing to design effective denoising and not only denoising algorithms.

The CDBM3D algorithm as well as its generalizations in [15-17] have a generic structure shown in Fig. 1. These algorithms are composed from two successive stages: thresholding and Wiener filtering. Each of these stages includes grouping, 3D/4D High-Order SVD (HOSVD) transform-domain spectra analysis of these groups, thresholding in the thresholding stage and Wiener filtering in the Wiener stage of these spectra and aggregations of the multiple estimates in order to get the final estimates for each stage. Full details of these algorithms and Wiener filtering can be seen in [15-17].

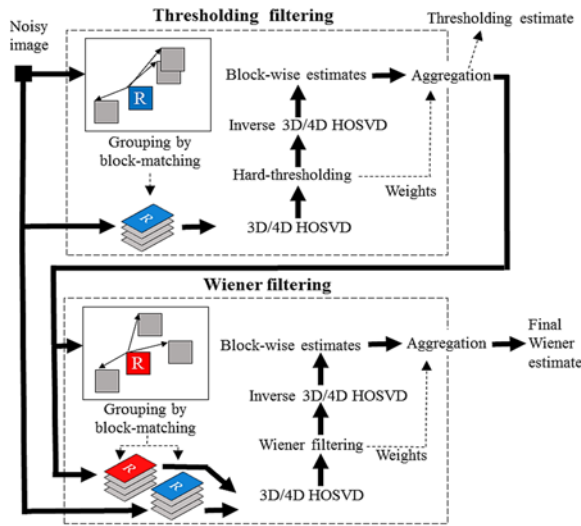


Fig. 1. A flow chart of CDBM3D algorithm.

3.2. Joint Denoising of HS Cube Slices

The second type of the algorithms considered in this paper is novel developed specifically for joint processing of all images of the HS cube or its fragments as defined by the estimate:

$$\hat{Q}_{\bar{\Lambda}}(x, y) = CCF\{Z_{\bar{\Lambda}}(x, y), \bar{\Lambda} \subset \Lambda\} \quad (3)$$

For instance, for windowed sliding filtering, $\bar{\Lambda}$ is an interval centered on $\lambda = \lambda_0$. As it is introduced above, it can be a wavelength symmetric interval of the width δ_{λ_0}

$$\bar{\Lambda} = \{\lambda : \lambda_0 - \delta_{\lambda_0}/2 \leq \lambda \leq \lambda_0 + \delta_{\lambda_0}/2\}.$$

The symbol *CCF* is an abbreviation for the Cube Complex domain Filter that processes all data of the

cube $Z_{\bar{\Lambda}}(x, y)$ jointly and returns the cube estimate $\hat{Q}_{\bar{\Lambda}}(x, y)$ for the all slices of the wavelength interval $\bar{\Lambda}$. The algorithm presented in this paper is an adaptation for the complex domain of the Fast Hyperspectral Denoising algorithm (FastHyDe) proposed for real-valued HS observations in [14].

The *CCF* algorithm is composed from the following steps.

1. Reshape 3D data cube $Z_{\bar{\Lambda}}, N \times M \times L_{\bar{\Lambda}}$, to the 2D matrix Z of the size $L_{\bar{\Lambda}} \times N \cdot M$. Note, that the each row of this matrix corresponds to $N \times M$ image in the cube $Z_{\bar{\Lambda}}$.

2. Applying SVD to the matrix $Z_{\bar{\Lambda}}$ we calculate the orthonormal square transform matrix $E \in \mathbb{C}^{L_{\bar{\Lambda}} \times L_{\bar{\Lambda}}}$ and the 2D transform domain eigenimage $Z_{2,eigen}$ as

$$[Z_{2,eigen}, E, k] = HySime(Z), \quad (4)$$

where *HySime* stays for Hyperspectral signal Subspace Identification by Minimum Error [21], and k is an optimal length of the eigenspace. *HySime* is an important part of the *CCF* algorithm. It identifies an optimal subspace for the sparse representation of HS image including both the dimension of the eigenspace k and eigenvectors - columns of E . The matrix $E_k \in \mathbb{C}^{L_{\bar{\Lambda}} \times k}$ in *HySime* is composed from the k main columns of E . When E_k is given, the k eigenimages are calculated in *HySime* as

$$Z_{2,eigen} = E_k^H Z \quad (5)$$

The *HySime* algorithm is based on the assumption that the slices $U(x, y, \lambda)$ for $\lambda \in \bar{\Lambda}$ are realizations of a random field.

3. Reshape the transform domain 2D image $Z_{2,eigen}, k \times N \cdot M$, to the 3D cube of the size $N \times M \times k$ with notation $Z_{3,eigen}$.

4. Filter by CDBM3D each of the k eigenimages, ($N \times M$) slices, of $Z_{3,eigen}$:

$$\hat{Z}_{3,eigen} = CDBM3D(Z_{3,eigen}) \quad (6)$$

5. Reshape the 3D cube $\hat{Z}_{3,eigen}$ to the 2D image $\hat{Z}_{2,eigen}$ of size $k \times N \cdot M$ and go from the eigenimages in the transform domain to images in the original image space by:

$$\hat{Z}_2 = E_k \hat{Z}_{2,eigen} \quad (7)$$

It is an inverse of the transform used in (5).

6. Reshape the 2D image \hat{Z}_2 to cube $N \times M \times L_{\bar{\Lambda}}$. It gives the result: the filtered HS cube $\hat{Q}_{\bar{\Lambda}}(x, y)$ (3).

The main point of this algorithm is that the transforms to eigenimage space (5) and backward return from the eigenspace to the image space (7) are produced as 2D matrix operation with the transform matrix E_k . The 2D filtering by CDBM3D (6) is produced for the k eigenspace images only.

Due to similarity of the HSI slices, the dimension k of the eigenspace is much smaller than the length $L_{\bar{\Lambda}}$ of the HS data-cube.

4. Simulation Tests

For modeling, we assume a transparent phase object with the amplitude equal to 1 and the phase calculated according to equation:

$$\Delta\varphi_\lambda(x, y) = \frac{2\pi}{\lambda}(n_\lambda - 1) \cdot h(x, y), \quad (8)$$

where n_λ is the wavelength dependent refractive index, λ is the wavelength, and $h(x, y)$ is the thickness of the object.

The refractive index n_λ is calculated for each wavelength according to the empirical Cauchy relationship, which is in a good agreement with measured data in a visible region of spectra. The coefficients of the relationship are taken assuming that the object material is the borosilicate BK7 glass.

For the thickness function $h(x, y)$, we took a truncated Gaussian peak (Fig. 2(a)) of the maximum equal to $4 \mu\text{m}$ which corresponds to the maximum phase delay of about 34 rad provided $\lambda = 400 \text{ nm}$, and $n_\lambda = 1.531$. The HS cube is modeled in accordance with (8) for 200 uniformly distributed wavelengths in the range of $\Lambda \in [400 - 798] \text{ nm}$.

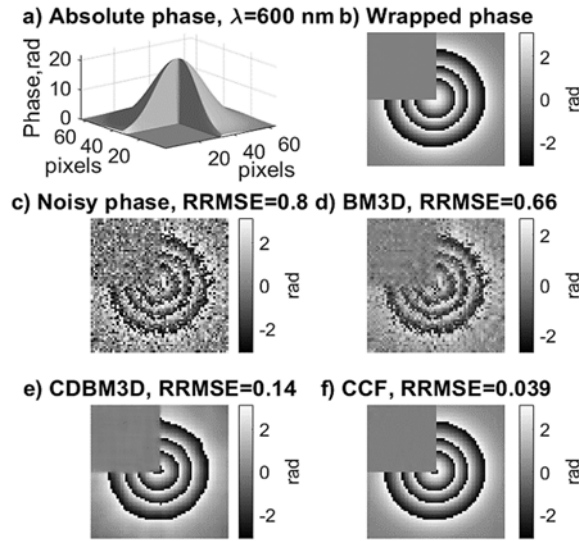


Fig. 2. Object phases of the slice $\lambda = 600 \text{ nm}$: clean absolute phase (a) and clean wrapped phase (b); noisy wrapped phase as it is observations (c); and phase reconstructions by BM3D (d), CDBM3D (e), and CCF (f).

For this thick object the absolute phase values exceed the interval of $[-\pi, \pi]$ and the observations depend on wrapped phase. For wrapped phase observations, HS phase imaging becomes a hard problem since the phases even in neighboring slices of the HS cube can be very different. Therefore, the widespread filtering by averaging nearest HS cube slices is not applicable. For filtering of wrapped phases, unwrapping procedures are used often. These procedures are computationally demanding and

sometimes not applicable, especially in high noise scenarios. However, the used CDBM3D filter is specially developed to work in complex-domain and able to produce reliable results for wrapped phase filtering without involving unwrapping procedures.

For quantitative estimation of the phase filtering accuracy, we use Relative Root Mean Square Error (RRMSE) criterion:

$$RRMSE = \frac{\sqrt{\sum_{x,y} |\hat{\varphi}(x, y) - \varphi(x, y)|^2}}{\sqrt{\sum_{x,y} |\varphi(x, y)|^2}}, \quad (9)$$

where $\varphi(x, y)$ is the clean wrapped phase, $\hat{\varphi}(x, y)$ is the reconstructed wrapped phase, (x, y) are the spatial coordinates, the summation is produced over all pixel of the images. RRMSE values close to 1 correspond to a bad noise suppression, RRMSE values smaller than 0.1 can be treated as a good quality imaging.

For comparison, we provide results obtained by the following state-of-the-art filtering techniques: BM3D, CDBM3D, and proposed CCF. BM3D is a wide spread technique based on non-local sparse representations, which produces good noise suppression in a real-domain space. Here, it is used for separate filtering of phase and amplitude of HS slices. CDBM3D is a descendant of BM3D developed for complex-domain space for joint processing of phase and amplitude in the complex valued field. Here, it is used for joint filtering of phase and amplitude of HS slices.

Visual results for the same slice, $\lambda_0 = 600 \text{ nm}$, and $\text{SNR} = -2 \text{ dB}$ are presented in Fig. 2. Figs. 2(a) and (b) show clear (true) absolute and wrapped phases of the object, Fig. 2(c) shows noisy wrapped phase as they define the observations, and Figs. 2(d,e,f) show the wrapped phases as they are reconstructed by the BM3D, CDBM3D, and CCF algorithms, respectively. The phase images in Fig. 2 demonstrate the obvious advantage of the proposed CCF technique. For BM3D, it is hard to find similar patches in the slice for such noisy case, consequently it fails. CDBM3D using complex valued data adaptive atoms for non-local sparse approximation of the estimated object is able to suppress noise better, but nevertheless the phase estimate is severely corrupted since some valuable information on the phase lost due to the noise. Due to the total HS cube processing, the CCF algorithm is able to suppress the noise effectively and retrieve object's details almost identically to the original ones, as can be seen in Fig. 2(f). A nearly perfect visually CCF filtering is supported by the low RRMSE value, which is equal to 0.039.

Fig. 3 demonstrates RRMSE curves for each of the compared algorithms depending on the signal-to-noise-ratio (SNR) for the wavelength $\lambda_0 = 600 \text{ nm}$. Higher SNR values correspond to less noisy data, $\text{SNR} = 30 \text{ dB}$ is nearly a noiseless case. As it is expected, all RRMSE curves in Fig. 3 behave similar: lower values of SNR correspond to higher noise level,

and therefore RRMSE are higher. However, BM3D (yellow stars curve) reaches values smaller than 0.1 only for SNR larger than 15, while CDBM3D (red circles) reaches 0.1 already for SNR about 4. The best performance is demonstrated by RRMSE corresponding to the *CCF* algorithm (blue crosses) with values under 0.1 even for extremely noisy case with SNR = -10 dB.

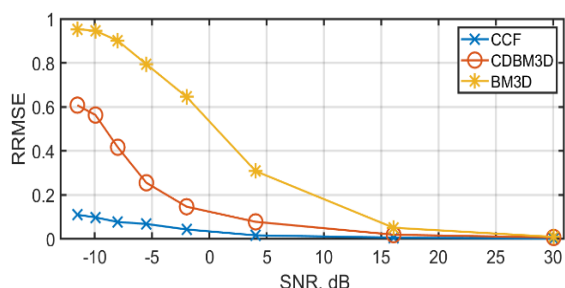


Fig. 3. RRMSE as functions of SNR. Comparison of the algorithm's performance: *CCF* – curve with blue crosses, CDBM3D - red circles, and BM3D - yellow stars.

It is interesting to evaluate a number of slices sufficient for noise suppression. For this purpose, we present in Fig. 4 a dependence of RRMSE from the number of slices in the HS cube and from SNR. It is done for the object shown in Fig. 2(a). The dark blue regions of this 3D surface with low RRMSE values correspond to the good filtering. It demonstrates, that for low noise level (high SNR) the RRMSE values do not depend strongly on the number of slices, therefore it is not necessary to use *CCF* for low noise cases. However, to get sufficient noise suppression for HS cubes with SNR lower than 10 dB, it is necessary to use the joint *CCF* processing and the number of slices in the HS cube should be larger than 100.

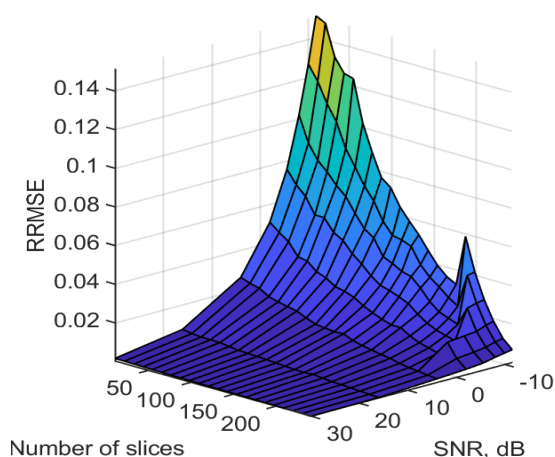


Fig. 4. RRMSE surface dependence from the number of slices in the HS data and SNR.

It is necessary to mention also that RRMSE depends on similarity of the slices and therefore on the spectral object properties. Nevertheless, RRMSEs will

have similar behavior for any type of objects. The only difference is in gradients of RRMSE surfaces: for simple objects (high similarity of the slices), the gradients will be smaller, for complex-structure objects (low similarity), the gradients will be higher since a high level of similarity provides better noise suppression.

5. Experimental Results

We use the experimental HS data obtained by the spectrally resolved digital holography (SRDH). The object is a transparent color slide shown in Fig. 5(a), and the light source is a white LED [7]. Fig. 5(b) shows the intensity spectrum of this LED in the range $\Lambda = [400 - 800]$ nm.

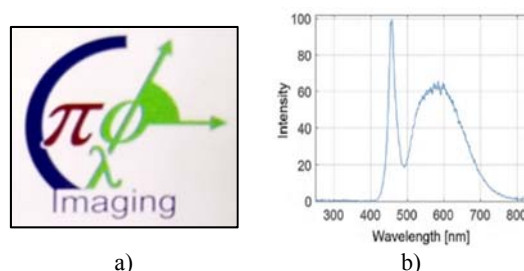


Fig. 5. a) Investigated object; b) LED spectra.

In systems, where digital cameras make intensity registration, the additive noise is inherent, and it is obvious, that SNR of the recorded intensities is lower in spectral ranges with smaller intensity of LED. For the used LED, low SNR regions are in the areas of 400 nm and 800 nm.

We demonstrate *CCF* filtering results in two spectral regions with high SNR (556 nm) and low SNR (780 nm). In Fig. 6 for the slice of the HS cube $Z(x, y, \lambda)$ corresponding to 556 nm wavelength λ and in Fig. 7 to 780 nm: the noisy phase and amplitude are in the top row and the ones filtered by *CCF* $\hat{U}(x, y, \lambda)$ are in the bottom row. In the region of high SNR, see Fig. 6, the noisy slice is only slightly corrupted. After *CCF* filtering, the amplitude and phase look much more clear, especially the phase image in low-intensity regions of amplitude (dark areas).

In contrast with the high SNR slice, the low SNR noisy slice in Fig. 7 is destroyed, and it is hard to distinguish observed object details in both amplitude and phase. However, after application of the *CCF* filter, we can clearly see the details of phase and amplitude images for $\hat{U}(x, y, \lambda)$ retrieved from the very noisy $Z(x, y, \lambda)$.

This result is a strong demonstration of the good performance of the proposed *CCF* algorithm. Such results are unattainable for traditional averaging of few neighboring slices or for the state-of-the-art techniques operating over single slices.

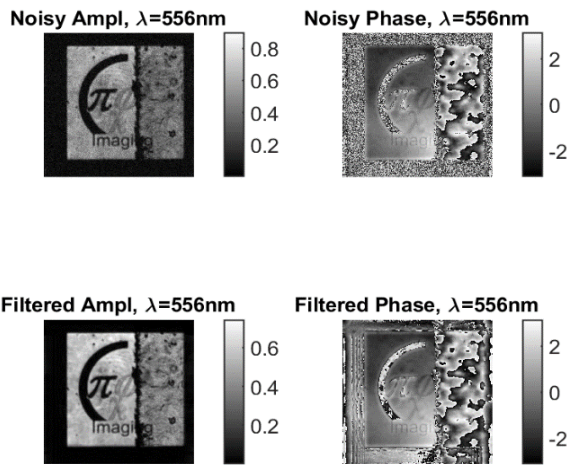


Fig. 6. Noisy and filtered object slices corresponding to 556 nm. Top row: images of noisy amplitude (left) and phase (right); bottom row: CCF filtered amplitude and phase in rad.

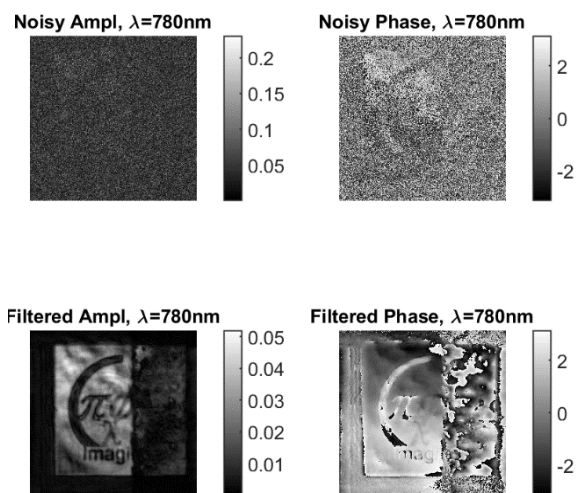


Fig. 7. Noisy and filtered object slices corresponding to 780 nm. Top row: images of noisy amplitude (left) and phase (right); bottom row: CCF filtered amplitude and phase in rad.

6. Conclusion

A new denoising algorithm for joint processing of broadband complex domain hyperspectral data is developed. The algorithm is robust and able to produce reliable noise suppression and reveal object details even in extremely noisy scenarios. The algorithm demonstrates a very good performance to filter wrapped phase HS data without involving unwrapping processing.

Acknowledgements

This work is supported by the Academy of Finland, project no. 287150, 2015-2019 and Horizon 2020 TWINN-2015, grant 687328 - HOLO.

References

- [1]. W. L. Wolfe, Introduction to Imaging Spectrometers, SPIE Press, Bellingham, Washington, 1997.
- [2]. A. F. H. Goetz, Three decades of hyperspectral remote sensing of the Earth: a personal view, *Remote Sensing of Environment*, Vol. 113, Suppl. 1, 2009, pp. S5–S16.
- [3]. M. Govender, K. Chetty, H. Bulcock, A review of hyperspectral remote sensing and its application in vegetation and water resource studies, *Water SA*, Vol. 33, Issue 2, 2007, pp. 145–151.
- [4]. Y. Z. Feng, D. W. Sun, Application of hyperspectral imaging in food safety inspection and control: a review, *Critical Reviews in Food Science and Nutrition*, Vol. 52, Issue 11, 2012, pp. 1039–1058.
- [5]. G. Lua, B. Fei, Medical hyperspectral imaging: a review, *Journal of Biomedical Optics*, Vol. 19, Issue 1, 2014, p. 010901.
- [6]. S. G. Kalenkov, G. S. Kalenkov, A. E. Shtanko, Hyperspectral holography: an alternative application of the Fourier transform spectrometer, *Journal of the Optical Society of America B*, Vol. 34, Issue 5, 2017, pp. B49–B55.
- [7]. D. Claus, G. Pedrini, D. Buchta, W. Osten, Accuracy enhanced and synthetic wavelength adjustable optical metrology via spectrally resolved digital holography, *Journal of the Optical Society of America A*, Vol. 35, Issue 4, 2018, pp. 546–552.
- [8]. M. S. Kulya, V. A. Semenova, V. G. Bespalov, N. V. Petrov, On terahertz pulsed broadband Gauss-Bessel beam free-space propagation, *Scientific Reports*, Vol. 8, Issue 1, 2018, p. 1390.
- [9]. V. Cazac, A. Meshalkin, E. Achimova, V. Abashkin, V. Katkovnik, I. Shevkunov, D. Claus, G. Pedrini, Surface relief and refractive index gratings patterned in chalcogenide glasses and studied by off-axis digital holography, *Applied Optics*, Vol. 57, 2018, pp. 507–513.
- [10]. V. Katkovnik, I. Shevkunov, N. V. Petrov, K. Egiazarian, Multiwavelength surface contouring from phase-coded diffraction patterns, *Proceedings of the SPIE - the International Society for Optical Engineering*, Vol. 10677, 2018, p. 106771B.
- [11]. V. Katkovnik, I. Shevkunov, N. V. Petrov, K. Egiazarian, Multiwavelength absolute phase retrieval from noisy diffractive patterns: wavelength multiplexing algorithm, *Applied Sciences*, Vol. 8, Issue 5, 2018, pp. 719.
- [12]. G. S. Kalenkov, S. G. Kalenkov, I. G. Meerovich, A. E. Shtanko, N. Yu. Zaalishvili, Hyperspectral holographic microscopy of bio-objects based on a modified Linnik interferometer, *Laser Physics*, Vol. 29, Issue 1, 2018, pp. 016201.
- [13]. V. Katkovnik, I. Shevkunov, D. Claus, G. Pedrini, K. Egiazarian, Non-local Similarity Complex Domain Denoising for Hyperspectral Phase Imaging, in *Proceedings of the 2nd International Conference on Optics, Photonics and Lasers (OPAL'2019)*, Amsterdam, The Netherlands, 24–26 April 2019, pp. 11–15.
- [14]. L. Zhuang, J. Bioucas-Dias, Fast hyperspectral image denoising and inpainting, *IEEE Journal of Selected Topics in Applied Earth Observations and Remote Sensing*, Vol. 11, Issue 3, 2018, pp. 730–742.
- [15]. V. Katkovnik, K. Egiazarian, Sparse phase imaging based on complex domain nonlocal BM3D techniques, *Digital Signal Processing*, Vol. 63, 2017, pp. 72–85.

- [16]. V. Katkovnik, M. Ponomarenko, K. Egiazarian, Sparse approximations in complex domain based on BM3D modeling, *Signal Processing*, Vol. 141, Issue C, 2017, pp. 96-108.
- [17]. V. Katkovnik, M. Ponomarenko, K. Egiazarian, Complex-valued image denoising based on group-wise complex-domain sparsity, arXiv preprint arXiv: 1711.00362v1, 2017.
- [18]. Matlab code for complex-domain noise filtering (CDBM3D),
url: <http://www.cs.tut.fi/sgn/imaging/sparse/cdid.zip>
- [19]. K. Dabov, A. Foi, V. Katkovnik, K. Egiazarian, Image denoising by sparse 3-D transform-domain collaborative filtering, *IEEE Transactions on Image Processing*, Vol. 16, Issue 8, 2007, pp. 2080-2095.
- [20]. V. Katkovnik, J. Astola, High-accuracy wave field reconstruction: decoupled inverse imaging with sparse modeling of phase and amplitude, *Journal of the Optical Society of America A*, Vol. 29, Issue 1, 2012, pp. 44-54.
- [21]. J. Bioucas-Dias, J. Nascimento, Hyperspectral subspace identification, *IEEE Transactions on Geoscience and Remote Sensing*, Vol. 46, Issue 8, 2008, pp. 2435-2445.



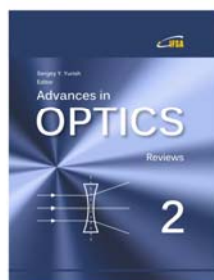
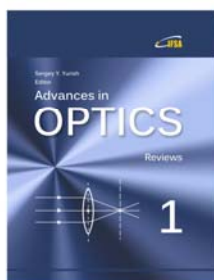
Published by International Frequency Sensor Association (IFSA) Publishing, S. L., 2019
(<http://www.sensorsportal.com>).

Your chapter may be in the next volume of the

Advances in OPTICS

Reviews

Open Access Book Series



 IFSA Publishing

http://www.sensorsportal.com/HTML/IFSA_Publishing.htm